Targeted Molecular Imaging of Cardiovascular Diseases by Iron Oxide Nanoparticles

Targeted Molecular Imaging of Cardiovascular Diseases by Iron Oxide Nanoparticles

Karla X. Vazquez-Prada[1,2,3], Jacinta Lam[3], Danielle Kamato[3], Zhi Ping Xu[1], Peter J. Little[2,5], Hang T. Ta[1,2,4,*]

[1] Australian Institute for Bioengineering and Nanotechnology, the University of Queensland, St Lucia, Queensland 4072, Australia

[2] Queensland Micro- and Nanotechnology, Griffith University, Brisbane, Australia

[3] School of Pharmacy, Pharmacy Australia Centre of Excellence, the University of Queensland, Woolloongabba, Queensland 4012, Australia

[4] School of Environment and Science, Griffith University, Brisbane, Australia

[5] Department of Pharmacy, Xinhua College of Sun Yat-sen University, Tianhe District, Guangzhou 510520, China

*** Correspondence:** Hang T. Ta (h.ta@griffith.edu.au)

Keywords: iron oxide, molecular imaging, cardiovascular diseases, magnetic resonance imaging

Abstract

Cardiovascular disease (CVD) is one of the major contributors to global disease burden. Atherosclerosis is an inflammatory process that involves the accumulation of lipids and fibrous elements in the large arteries, forming an atherosclerotic plaque. Rupture of unstable plaques leads to thrombosis that triggers life-threatening complications such as myocardial infarction. Current diagnostic methods are invasive as they require insertion of a catheter into the coronary artery. Molecular imaging techniques such as magnetic resonance imaging (MRI) have been developed to image atherosclerotic plaques and thrombosis due to its high spatial resolution and safety. The sensitivity of MRI can be improved with contrast agents, such as iron oxide nanoparticles. This review presents the most recent advances in atherosclerosis, thrombosis, and myocardial infarction molecular imaging using iron oxide-based nanoparticles. While some studies have shown their effectiveness, many are yet to undertake comprehensive testing of biocompatibility. There are still potential hazards to address and complications to diagnosis, therefore strategies for overcoming these challenges are required.

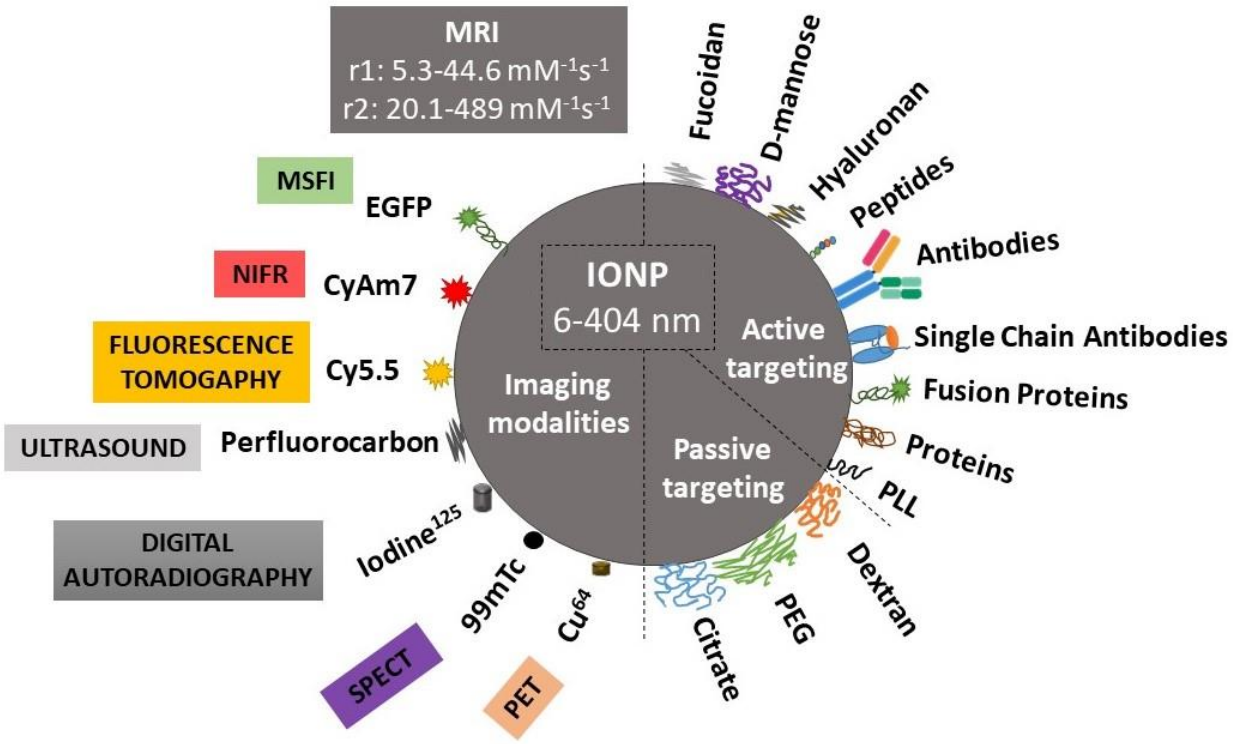
MRI
r1: 5.3-44.6 mM-1s-1
r2: 20.1-489 mM-1s-1
MSFI
EGFP
NIFR
CyAm7
FLUORESCENCE TOMOGAPHY
Cy5.5
ULTRASOUND
Perfluorocarbon
DIGITAL AUTORADIOGRAPHY
Iodine125
99mTc
Cu64
SPECT
PET
IONP
6-404 nm
Imaging modalities
Active targeting
Passive targeting
Fucoidan
D-mannose
Hyaluronan
Peptides
Antibodies
Single Chain Antibodies
Fusion Proteins
Proteins
PLL
Dextran
PEG
Citrate

1. Introduction

CVD is the leading cause of morbidity and mortality worldwide, with an estimated 31% of global deaths(1). The underlying causes of mortality in CVD include heart attacks and strokes, which are caused by a vascular blockage that prevents blood from flowing to the heart or brain (1-3). This is caused by the localized clotting of blood occurring in the arterial and venous circulation referred as thrombosis (4).

Arterial thrombosis often results from thromboembolism or a complication of atherosclerosis, a multifactorial immunoinflammatory disease characterized by lesions in aortic tissue caused by LDL-cholesterol retention to proteoglycans (5). Macrophages uptake ox-LDL and contribute to foam cell formation (6). The death of these cells results in apoptotic cores full of thrombotic material. Rupture of unstable plaques releases these materials, activating the coagulation cascade and resulting in thrombus formation, which can lead to myocardial infarction (MI) (Figure 1A) (2,3,7,8) and an ischemic stroke (9).

Venous thromboembolism (VTE) can be divided into deep-vein thrombosis (DVT) and pulmonary embolism (PE) (10). DVT describes thrombus in the deep venous system (Figure 1B). The majority of deep-vein thrombi originate from thigh and lower leg veins. PE occurs when a deep-vein thrombus detaches and reaches the lungs. The embolus subsequently impairs the gas exchange and circulation in the lung (11). This causes ventilation-perfusion mis-match in the alveoli, and the activated platelets release serotonin and thromboxane (12). These changes trigger vasoconstriction in the unaffected areas, increasing the pulmonary artery systolic pressure and right ventricular after load, leading to right ventricular failure (10).

Thrombosis can range from an asymptomatic condition to a medical condition of swelling, edema, reddish discolouration and discomfort, which hampers a clinical evaluation and diagnosis based on symptomatology (13). Symptoms of MI include chest pain, shortness of breath, and abnormal heart beating (14). Atherosclerosis is asymptomatic in early stages until the plaques grow and arterial lumen is reduced (15). Early diagnosis and rapid treatment of CVDs is fundamental to decrease mortality and recurrence (14). Diagnosis of CVDs is achieved by cardiovascular imaging using techniques like ultrasound, angiography, venography, optical coherence tomography, and computer tomography (CT) (16).These techniques are associated with disadvantages such as invasiveness, the use of ionizing radiation and toxic contrasts that can cause side effects like nephropathies. Moreover, images can only be reconstructed for a selected phase of the cardiac cycle or have limited accuracy and specificity (17,18).

Contrast agents could be labelled with targeting molecules that can specifically bind to biomarkers of the biological processes or disease sites, allowing low dose molecular imaging solutions and enhancing lesion detectability. Iron oxide nanoparticles (IONPs) have been widely studied and developed as imaging agents for diagnosis of diseases (19-23). IONPs are also known as supermagnetic iron oxide nanoparticles (SPIONs) because of their excellent magnetic applications (24-28). SPIONs can alter the intrinsic contrast properties of biological tissues (1) directly by changing the proton density of a tissue, and (2) indirectly by altering the relaxation properties of surrounding hydrogen protons, changing local magnetic field or the resonance properties of a tissue and hence its relaxation time T_2 values (16,24,29). In T_2-weighted imaging, the magnetic moments of unpaired electrons from the MRI contrast agents alter the local magnetic field strength, resulting in faster dephasing due to spin-spin effects, hence a shorter T_2 value. Relaxivity is a measure of the change in the relaxation rate of hydrogen protons as a function of contrast agent's concentration and it is required to compare the efficacy of different IONPs as MRI contrast agents (30). Here, we summarize the

paramount findings in molecular imaging of atherosclerosis, thrombosis and MI using IONPs as targeted contrast agents.

2. Passively targeted IONPs as contrast agents for molecular imaging of atherosclerosis and thrombosis

IONPs are eliminated by phagocytosis via the monocyte-macrophage system, suggesting they could accumulate where inflammatory responses are present, such as human atherosclerotic plaques and thrombi (31). Studies in ApoE (-/-) mice demonstrate uptake of IONPs by macrophages. Macrophage uptake of citrate-coated IONPs was assessed at different stages of plaque development in the brachiocephalic artery (32). Citrate-IONPs were injected 24 and 48h prior to the scans. Susceptibility gradient mapping magnetic resonance imaging (SGM-MRI) showed an increase of citrate-IONPs uptake with the progression of plaque development. Similar data were obtained from histology and mass spectroscopy analyses.

The coating of IONPs is of tremendous importance for the circulating time of the nanoparticles (33). Generally, it was found that coating the nanomaterials with polyethylene glycol (PEG) shielded the surface from aggregation, opsonization and phagocytosis, prolonging systemic circulation time of the materials (34). Surprisingly, in the study of Ishida et al., coating with PEG has shown to increase the accelerated blood clearance effect (ABC) (35). In a murine model of peripheral arterial disease, PEGylated reduced-graphene oxide iron oxide nanoparticles (RGO-IONP-PEG) were used as carriers of ^{64}Cu, a radioisotope for positron emission tomography (PET) (36). PET imaging was performed at longitudinally after inducing hind limb ischemia in the mice. Animals were subdivided into mice that were used at each time point (naïve group), and mice that were repeatedly injected with the nanoparticles. Results showed effective accumulation of ^{64}Cu-RGO-IONP-PEG in the ischemic hindlimb at 24h post-injection. After 10 and 17 days post-surgery, the naïve group showed prolonged blood pool uptake while the treated group rapidly cleared up the nanoparticles from circulation. In addition, the uptake of ^{64}Cu-RGO-IONP-PEG in the disease site was lower in re-injected mice, and there was higher liver uptake in the reinjected group compared to the naïve group. The re-exposure of PEGylated RGO-IONP induces the ABC phenomenon and decreases the circulation half-life and passive targeting capabilities of ^{64}Cu-RGO-IONP-PEG. Hematoxylin and eosin (H&E) staining revealed that the nanoparticles accumulated in the Kupffer cells and other phagocytic cells of the liver was much higher in the re-injected group. This is likely explained by the anti-PEG immunoglobulin M (IgM) and complement activation-mediated clearance of PEGylated nanomaterials. Production of anti-PEG IgM occurs in response to the injection of ^{64}Cu-RGO-IONP-PEG. When the mice were re-injected with the ^{64}Cu-RGO-IONP-PEG, the nanoparticles are quickly recognized by the anti-PEG IgM, resulting in complement activation and removal of the nanomaterials by the phagocytic system.

Another follow-up study (37) assessed the enhanced permeability and retention (EPR) effect in peripheral arterial disease using a similar ischemia model. PET imaging showed that nanoparticle accumulation was the highest at day 3 and the lowest at day 17, while serial laser Doppler imaging showed that blood perfusion in the femoral artery decreased at day 3 and 10 but was improved at day 17 post-surgery. The nanoparticles accumulated in ischemic tissues via EPR effect, which reduced as blood flow was normalized. These studies revealed that passive-targeting of RGO-IONPs is a promising approach for multimodal imaging of CVDs.

3. Actively targeted IONPs for molecular imaging of atherosclerosis, thrombosis and myocardial infarction

The surface of IONPs can be conjugated with ligands to enable site-specific interactions and enhance its delivery to the target of interest. (38). While passive targeting relies on the leakiness of blood vessels and passive diffusion, active targeting employs the attachment of binding ligands on the surface of the materials, allowing their specific binding to the surface markers of a target cell or tissue, improving specificity and efficiency of the contrast (39). Recently, enormous progress has been made for targeting nanocarriers to improve therapeutic outcome and decrease systemic toxicity.

3.1 Targeting monocytes/macrophages with dextran

Infiltration and accumulation of macrophages happen during the progression of atherosclerosis, thrombosis and MI, making them a potential target for non-invasive techniques (7,13). Targeting macrophages is often achieved by surface modification of IONPs with dextran, leveraging the expression of dextran-binding C-type lectins on the macrophage surface (40).

Ferumoxytol (FH) is used for the treatment of anaemia, but has gained interest as contrast agent for MRI (41). Yilmaz et al. (41) evaluated whether FH allows a better MRI characterization of infarct pathology than Gadolinium-based agents in a clinical trial for fourteen patients with acute MI. Baseline CMR was performed within 48 h to 7 days after the cardiac symptoms. Patients in this study had acute ST-elevation myocardial infarction caused by coronary artery occlusion or plaque rupture and an ischaemic cause of myocardial damage. FH was intravenously administered (17 mL FH containing 510 mg Fe) 24 h after the baseline CMR study. Then, patients underwent post-FH studies 48 h after FH administration. Analyses suggest that FH gave a more detailed analysis of MI mainly by macrophage infiltration, and hence might provide a better profile for evaluating MI than Gd-based agents.

Sosnovik et al. (42) showed that imaging of macrophages was possible in mice using magneto fluorescent nanoparticles (CLIO-Cy5.5) made of dextran-cross-linked iron oxide (CLIO) and Cy5.5. MI was induced by ligation of the left coronary artery in 12 mice and sham surgery was performed in 7 mice as a control. CLIO-Cy5.5 were injected after surgery and fluorescence tomography and MRI were performed 48 h post injection. MR images showed an increase in contrast-to-noise ratio in the infarcted mice (23.0±2.7), but not in the sham-operated mice (5.43±2.4). The fluorescence intensity of the infarcted mice (19.1±5.2) was greater than that of the control (5.3±1.4). CLIO have also been used as carriers of CyAm7 (43) for detecting vulnerable atherosclerotic plaques with near-infrared fluorescence (NIRF) microscopy. CLIO-CyAm7 accumulated in the superficial intima and within plaque macrophages, ECs and SMCs with impaired endothelial barrier function, suggesting that vulnerable plaques exhibit impaired endothelial permeability, leading to higher nanoparticle uptake. Histology findings are also consistent with the uptake of CLIO-Cy5.5 by tissue macrophages as the excised hearts revealed the infiltration of inflammatory cells into the infarcted myocardium on H&E staining.

Dextran-IONPs as carriers of iodine-125 for digital autoradiography of atherosclerotic plaques was also studied in ApoE(-/-) mice (44). The nanoparticles demonstrated high radiolabelling stability and long blood circulation time, leading to higher uptake in the heart of ApoE (-/-) mice compared to control. Digital autoradiography exhibited enhanced signals from the heart of ApoE (-/-) mice, peaking at 72h after administration of the nanoparticles.

Kao et al. (45) used monocyte chemoattractant protein-1 (MCP-1) motif to coat spherical iron oxide magnetic nanoparticles and target monocytes in atherosclerotic plaques. MRI was performed in ApoE (-/-) mice 40 h post-administration. *In vivo* images of the aorta showed an increase in the degree of darkness in mice fed with a high-fat diet for a longer time. A decrease

of pixel density in non-fat fed mice of 25.4% and 26.5% (wild-type mice and ApoE (-/-) mice, respectively) was shown while a decrease of 38.1% and 40.9% (ApoE (-/-) mice fed with high-fat diet for 2 and 4 days, respectively) was observed. Histology data confirmed that the kidney was the major organ employed for excreting the nanoparticles and that MCP-1-motif MNPs accumulated in vulnerable atherosclerotic plaques, indicating the potential affinity of MCP-1-motif MNPs in the atherosclerosis model.

3.2 Targeting monocytes/macrophages with other moieties

Active targeting of macrophages can be accomplished by conjugation with osteopontin targeting agents. Osteopontin is overexpressed by foamy macrophages in atherosclerotic plaques (46). Qiao *et al*. (47) developed Cy5.5-labeled osteopontin antibody-DMSA-coated IONPs (Cy5.5-OPN-DMSA-IONPs for MRI/optical dual-modality imaging. H&E, Masson's trichrome and immunofluorescence staining revealed the expression of OPN in atherosclerotic plaques. These nanoparticles enhanced T_2 contrast *in vivo* in ApoE (-/-) mice with a mean post/pre signal ratio of 0.64 compared to the control.

Tenascin-C, highly expressed in monocytes and macrophages, leads to inflammation and plaque rupture (48). Li et al. (49) developed anti-tenascin-C antibody USPIOs for evaluating the vulnerability of atherosclerotic plaques in ApoE (-/-) mice. Mice were either injected with anti-tenascin-C USPIO or with non-targeted USPIO. The MR images were taken before injection and after 16 and 24 weeks. At 16 weeks, the relative signal intensity in the targeted group was reduced by 15.7% which was more than that of the control group (reduced by 3.4%). Similar results were seen at 24 weeks, where the relative signal intensity changes in the targeted and the control group were -26.4% and -11.1%, respectively. Histopathological analyses demonstrated atherosclerotic plaque formation and confirmed that Tenascin-C expression of the plaques at 24 weeks was higher than that at 16 weeks (0.22 ± 0.04 vs. 0.13 ± 0.02, $P < 0.05$).

Hyaluronan is an endogenous ligand for CD44, an adhesion protein expressed on cells involved in atherosclerosis such as macrophages (50). The effect of the morphology of hyaluronan-conjugated iron oxide nanoworms (HA-NWs) and hyaluronan-conjugated-SPIONs (HA-SPIONs)on inflammatory responses of atherosclerotic plaques was studied in ApoE(-/-) mice (51). HA-NW has an elongated shape whereas HA-SPIONs is a spherical. The mice were injected with HA-SPIONs and HA-NWs and T_2*-weighted images were obtained before and post-injection. Administration of HA-NW caused T_2* signal intensity of the aorta wall to reduce by 20% of pre-injection levels at 20 min after injection and this effect was sustained for over 120 min. HA-SPIONs caused significant MR signal losses and the intensities of lumen did not recover even after 140 min, preventing the detection of plaques on aorta walls due to a lack of MR contrasts between the lumen and aorta walls. The result indicated that nanomaterial shape is important for targeting to blood vessel wall, which is consistent with other reports (52). HA-NWs were less toxic as shown by lower cytokine levels in RAW 364.7 cells, probably because low molecular weight HA can produce inflammatory responses, while the high molecular weight HA are anti-inflammatory. CD44 binding affinity to HA is dependent on the molecular weight and it significantly increases with higher molecular weight of HA. Considering that one nanoworm consists of multiple SPIONs, it is possible that the elongated structure of the SPIONs arranged together can better mimic high molecular weight HA and reduce the inflammatory responses generated by the iron oxide core of the nanoprobes. These results indicate that HA-NWs were not only safer, but also more superior imaging agents than HA-SPIONs.

CD163 is a membrane receptor expressed by macrophages and is associated with plaque progression in atherosclerotic lesions. CD163-targeted gold-coated-IONPs were tested as

contrast agents for detection of atherosclerotic plaques in ApoE(-/-) mice (53). Imunohistochemistry validation confirmed all the mice had atherosclerotic lesions in the MRI scanned area and that the plaques were composed by a layer of smooth muscle cells with small lipid deposits and infiltrated macrophages. MRI was performed before and after administration. The MR images showed a decrease in T_2 signal at 24h, which became significant at 48h, providing evidence that the nanoparticles were able to enhance the visualization of atherosclerotic plaques and their targeting of macrophages with CD163 was successful.

Annexin V is used to target apoptotic macrophages in vulnerable plaques, as it binds to phosphatidylserine (54). Cheng *et al*. (55) reported a hybrid-nanosystem for imaging using a single-photon-emission computed tomography (SPECT)/MRI multimodal probe. The nanosystem consisted of PEG-USPIOs functionalized with diethylenetriaminepentacetate acid for (99m)Tc coordination and Annexin V (99mTc−DTPA−USPIO−Annexin V) for targeting purposes. SPECT and MRI images in mice were consistent and showed an accumulation of the probes in vulnerable atherosclerotic plaques. Absorption of 99mTc−DTPA−USPIO−Annexin V by apoptotic macrophages lead to an enhancement of T_2-weighted MRI. A signal change of atherosclerotic plaques can be observed at 8h post-injection. Lesions in the aorta can be outlined when integrated with the MR images taken before the injection, improving the focal localization and volumetry of atherosclerotic plaques. Moreover, radioactive signals detected by SPECT facilitated focus recognition and quantification of vulnerable atherosclerotic plaques. Targeting effects were further confirmed by CD-68 and TUNEL staining. Results suggest that the Annexin V-modified hybrid nanoparticle system specifically targeted the vulnerable atherosclerotic plaques containing apoptotic macrophages.

Mannose receptors are over-expressed in some activated macrophages in rupture-prone atherosclerotic plaques and can potentially be used for effective targeting (56). Babič et al. (57) tested different nanoparticles (Resovist®, **γ-**Fe_2O_3, and **γ-**Fe_2O_3) coated with either D-mannose or poly(L-lysine) (PLL). *In vitro* MRI showed an increase in relaxivity after incubating the macrophages in nanoparticle-containing medium for 3h, which continued to increase until 24h). Intraperitoneal injection with D-mannose and (PLL)-γ-Fe_2O_3 nanoparticles in Prague hereditary hypercholesterolemic (PHHC) rats exhibited signal loss in the abdominal cavity immediately but disappeared 24h after administration. Even though viability and relaxivity of both nanoparticles were similar, PLL-γ-Fe_2O_3 nanoparticles were considered optimal, as the D-mannose might be more easily metabolized, exposing the uncoated iron oxide cores to the cell environment.

3.3 Targeting Endothelial Cells (ECs)

ECs constitute one of the essential components of the circulatory system and thus are an important element to consider for targeting CVDs. E-selectin, an adhesion protein expressed only on ECs activated by cytokines, was used to target ECs (58). CLIO nanoparticles were conjugated with an anti-human E-selectin (CD62E) F(ab')(2) fragment to form CLIO-F(ab')(2). Feasibility of CLIO-F(ab')(2) as MRI endothelial pro-inflammatory markers *in vitro* using human endothelial umbilical vein cells (HUVEC) was assessed. HUVECs were implanted in athymic mice in matrigel solution and were treated with interleukin 1 beta (IL-1β) and to express E-selectin. The formation of HUVEC-containing vessels was confirmed by histology and microscopy. Vessels that were highly positively stained for iron were detected only in matrigel implants initially seeded with HUVECs. Treated HUVECs showed 100-200 times higher binding to the nanoparticles than control cells. MRI showed that the cells treated with IL-1β also had a specific T_2-weighted signal darkening, suggesting that the system could be of potential use in monitoring diseases such as atherosclerosis.

Ex vivo MRI of CLIO-F(ab')(2) was tested using a model of HUVEC transfer to test specific imaging probes for human vascular disease (59). Animals harbouring HUVEC-containing matrigel implants and blank matrigel implants were sacrificed longitudinally after implantation. The implants were dissected without perfusion and analysed by histology and microscopy. Immunohistochemical staining for VEGFR-2 and CD31 indicated the successful and specific conjunction of anti-VEGFR-2 antibodies onto the nanoparticles. The CLIO-F(ab')(2) were injected following the induction of E-selectin expression with IL-1β and hypointensity was found only if treated with the interleukin. MRI images were taken pre- and post-injection of CLIO-F(ab')(2). Analyses showed a three-fold decrease in T2* images measured in HUVEC implants in response to IL-1β treatment. These observations support the *in vitro* findings and suggest that IL-1β-induced E-selectin expression in this HUVEC model is detectable by MRI using CLIO-F(ab')(2).

Vascular endothelial growth factor receptor 2 (VEGFR2) stimulates neoangiogenesis, which promotes infiltration of macrophages, thickening of the vessel wall, deposition of lipids, inflammation, atherosclerotic plaque progression and rupture (60). A nanosystem consisting of VEGFR2-targeted perfluorocarbon magnetic nanocapsules was designed for dual-modality imaging of atherosclerotic neovasculature (61). In the study, perfluorooctyl bromide (PFOB) was used as an ultrasound contrast agent. Ultrasound imaging was performed before and after injecting the nanocapsules in atherosclerotic rats. MR images were obtained prior to and post-injection. Ultrasound images showed echogenicity in the atherosclerotic/targeted group (65.1 dB) but not in the atherosclerotic/non-targeted (46.7 dB) or control/targeted group (46.0 dB). Similarly, the nanocapsules significantly attenuated the MRI contrast-to-noise ratio in the atherosclerotic/targeted group (74.2), but not in the atherosclerotic/non-targeted (48.9) or control/targeted group (46.9).

3.4 Targeting Vascular Smooth Muscle Cells (VSMCs)

VSMCs are another component of the vascular wall with a key role in the progression of many CVDs. Targeting VSMCs can be achieved by targeting profilin-1, an actin-binding protein that regulates VSMCs' proliferation and migration. Notably, its overexpression can lead to atherosclerosis (62). Profilin-1 targeted IONPs (PC-NPs) were synthesized for MR and fluorescence dual-modality imaging (63). *In vivo* MR and NIRF imaging were performed in ApoE (-/-) mice before and 36h after administration of nanoparticles. Compared to the non-targeted group, the fluorescence signal of the carotid artery was significantly higher in the targeted group. Similarly, the T_2 signal was significantly attenuated 36h post injection and the contrast to noise ratio (CNR) was significantly reduced in the targeted group (31.7%) compared to the non-targeted group (9.47%). Histology verification showed more nanoparticles deposited in atherosclerotic lesions of targeted group than those in other groups.

3.5 Targeting Activated platelets

Platelets contribute to not only thrombus formation, but also the inflammatory processes that affect atherosclerotic plaque development (12). Targeting activated platelets for molecular imaging was explored by Ta et al. (29,64-66). They developed a two-step chemoenzymatic coupling method for site-specific conjugation of a single-chain antibody (scFv) against LIBS epitopes on glycoprotein IIb/IIIa. *In vitro* adhesion assays and *in vivo* experiments in C57BL/6 wild type mice suggest that the scFv was successfully conjugated to the particles. Flow cytometry assays confirmed the specific binding of scFv to activated platelets and nonbinding to nonactivated platelets. Furthermore, there was an enhancement in T2*-weighed images for the detection of thrombosis in mice. Histological analysis of the injured carotid artery demonstrated MPIOs that bound on the induced thrombus.

Multimodal IONPs for targeted MRI of atherothrombosis was developed recently (16). The dual contrast IONPs (DCION2(+)) acted as positive and negative contrast agents. DCION2(+) were functionalized with single-chain antibodies (scFv) directed against activated platelets for molecular MRI and labelled with fluorescent molecules for optical imaging purposes. The targeting of DCION2(+) to activated GPIIb/IIIa receptors was demonstrated *in vitro* with receptor-expressing CHO cells and with activated platelets. Results show that DCION2(+) were able to shorten both T_1- and T_2 relaxation times. MR imaging of the thrombi *in vitro* showed contrast in T_1- and T_2-weighted imaging and demonstrated the efficient binding of DCION2(+) on the thrombi. The dual contrast was shown by a bright ring around the thrombi in T_1-weighted images, and by a dark ring around the thrombi in T_2-weighted images. *In vivo* MRI showed the largest change in signal at 70 min post-injection and a gradual decline after this time point. Ex vivo fluorescence imaging confirmed the specific binding of DCION2(+) to thrombus.

VUSPIOs differ from SPIONs by its functionalization with aminated polysiloxane film grafted on their surface and embedded in a dextran corona. Versatile ultra-small super-paramagnetic nanoparticles (VUSPIOs were functionalized with recombinant human IgG4 antibody (rIgG4 TEG4) to target platelet membrane glycoproteins αIIB and β3 (67). Staining of macrophages by anti-CD68 antibody was performed to show the localisation of platelets. Results show an accumulation of nanoparticles in areas of foam cells and platelet-leucocytes-aggregates. Transversal relaxivity of the nanoparticles was found to be 273 mM^{-1} s^{-1} in the presence of platelets and 257 mM^{-1} s^{-1} when measured alone. *Ex vivo* MRI of the aorta of mice injected with the TEG4-VUSPIO showed a selective binding of TEG4-VUSPIO on atheroma plaques which induced a loss of MRI signal, whereas no loss of signal was observed in mice injected with IgG-USPIOs.

Another platelet-targeting IONPs were coated with fucoidan (USPIO-FUCO), a sulphated polysaccharide having high affinity for P-selectin (68). Suzuki et al. (69) synthesized USPIO-FUCO and found that the nanoparticles bound to P-selectin *in vitro*. *In vivo* thrombi could be evidenced by MRI on animals injected with the USPIO-FUCO. Importantly, there was no variation in signal post-injection with control USPIO nanoparticles after 2 h. MRI of thrombi were correlated with P-selectin immunostaining and USPIO detection by electron microscopy. Data suggest that an effective targeting to activated platelets was achieved in *in vivo* MRI thrombi imaging (Figure 3).

Arg-Gly-Asp (RGD) domain is a cell adhesion motif present in many integrins and matrix molecules, including GIIb/GIIIa (70). Targeting activated platelets through GIIb/GIIIa with cRGD conjugated PLGA-IONPs for detection of thrombosis was reported (71). The PLGA-IONPs-cRGD were tested *in vivo* using a rat model of $FeCl_3$-induced abdominal aorta thrombosis. *In vivo* and *ex vivo* biodistribution indicated that the nanoparticles accumulated selectively on the surface of the thrombi and were internalized by macrophages in the liver and the spleen. Moreover, *in vivo* MRI data showed a decrease in T_2 signal at the thrombus 10 min after injection and a gradual increase until 50 min, suggesting that this nanosystem might represent a promising contrast agent for specific detection of thrombosis.

Fusion proteins such as enhanced fluorescent protein-epidermal growth factor 1 (EGFP-EGF1) have recently gained interest as they can be conjugated in nanomaterials with the purpose of providing targeting moieties and contrast ability. Epidermal growth factor 1 (EGF1) binds to the tissue factor present in activated platelets whereas enhanced green fluorescent protein (EGFP) provides fluorescence. Hu et al. (72) synthesized EGFP-EGF1 to target activated platelets for dual molecular imaging of cerebral thrombosis (72). *In vivo* multispectral

fluorescence imaging (MSFI) validated the targeting efficiency of EGFP-EGF1-IONPs. The nanoparticles were mainly accumulated in the tissue factor exposure region of the brain, suggesting EGFP-EGF1-IONPs might be a feasible contrast agent for the early diagnosis of cerebral thrombosis. Although the authors did not present any data of MRI studies, it might be worth conducting MRI analyses in a follow-up study, as the nanosystem is based on IONPs, which are known to be contrast agents for MRI.

3.6 Targeting Fibrin

Fibrin is a key component of thrombi and a crucial factor in atherosclerosis (73). An IONP-micelle system was functionalized with fibrin-binding peptides (FibPeps) for the detection of thrombi (74). Thrombus detection by FibPep-ION-Micelles was studied in a mouse model of carotid artery thrombosis with *in vivo* quantitative MRI. Histological analysis confirmed the occlusion of the injured carotid arteries and the absence of occlusion in the contralateral, non-injured carotid arteries. Thrombus uptake of FibPep-ION-Micelles and measurements of the carotid arteries were performed *ex vivo* using a magnetic particle spectrometer (MPS). FibPep-ION-Micelles showed decreased T_2 value in the thrombus area (22.7 ± 1.5 ms) in comparison with the pre-injection value (26.5 ± 2.6 ms). *Ex vivo* MPS confirmed an increased thrombus signal compared with the non-injured control. In contrast, there was no increase in MPS thrombus signal for the FibPep-ION-Micelles when compared to the non-targeted micelles, suggesting the uptake of the nanoparticles by the thrombi might be due to entrapment. Thus non-targeted ION-Micelles might be of value for diagnosis of thrombosis.

One of the peptide molecules used to target fibrin is CREKA due to its interactions with fibrin-fibronectin complexes (75). Spherical hybrid metal oxide-peptide amphiphile micelles were developed for molecular MRI of human clots (76). The micelles consisted of an iron oxide core and were functionalized with fibrin-targeting peptide amphiphiles with the sequence CREKA. Studies with *in vitro* clots showed that the signal intensity of MR images with targeted micelles was 65% compared to 35% for non-targeted, exhibiting a two-fold T_2 signal enhancement.

Ta et al. (77,78) designed a MRI nanosensor to distinguish age of thrombus. The nanosensor consisted of IONPs coated with a detachable layer of Gd and functionalized with peptide targeting fibrin, which is present on both fresh and old thrombi. If the nanosensor binds to a fresh thrombus, thrombin (present only in fresh thrombus) will release the Gd from the IONPs, restoring T_1 signal. On the other hand, if the thrombus is old it will remain intact and it will possess T_2 signal. Results show that the absence of thrombin generated low r_1 values while in the presence of thrombin, r_1 increased significantly. In addition, the absence of thrombin exhibited high r_2 values, showing that IONPs are useful not only to detect thrombi, but also to estimate its age.

In summary, these studies demonstrate that IONPs can be functionalized with ligands to target different features of atherosclerotic plaques and thrombotic events, including VSMCs, ECs, monocytes, macrophages, platelets, and fibrin. The targeted-IONPs successfully accumulate in the region of interest and can enhance MR images by significantly inducing contrast.

4. *In vitro* and *In vivo* Toxicity of IONPs

IONPs are the most used nanoparticles for biomedical purposes, including the diagnosis of disease. Nonetheless, the understanding of their interactions with biological systems, toxicity, and uptake mechanisms is limited and is a field of major interest. The toxicity and biocompatibility of most of the nanoparticles reviewed above has been assessed *in vitro* and *in vivo*.

Murine 4T1 breast cancer cells were used to test *in vitro* toxicity of passive-targeted RGO–IONP–PEG using the MTT assay. The cells were incubated for 24h with different concentrations of RGO–IONP–PEG and no obvious toxicity was seen. Reactive oxygen species (ROS) were measured by dichlorodihydrofluorescein diacetate staining and used as an indicator of oxidative stress in RGO–IONP–PEG incubated cells. Results showed no generation of ROS even at the highest concentration tested (200 $\mu g.mL^{-1}$). Moreover, mice treated with RGO–IONP–PEG (200 μL, 2 $mg.mL^{-1}$) after photothermal therapy survived over a period of 40 days without a single death, showing no sign of toxicity nor significant body weight loss (79). Histological examination of major organs showed no apparent damage or abnormality, suggesting that RGO–IONP–PEG was not toxic to mice with these concentrations. On the other hand, other studies suggest that RGO may have potential interaction with serum proteins and induce intracellular ROS, which has limited the clinical translation of this nanoplatform (36).

Cytotoxicity of dextran- IONPs such as FH and FC has been assessed *in vitro* (41). Incubation of macrophages for 24h with FH (0.5 mg Fe/mL) and the lower concentration FC (0.25 mg Fe/mL) did not result in significant morphological changes and was not toxic, whereas incubation with higher concentration FC (0.5 mg Fe/mL) resulted in rapid cell death. Biodistribution study of dextran-IONPs as carriers of iodine-125 targeting mouse atherosclerotic plaques (100 μL, 10 μCi, 0.2 mg Fe/mL) show that the nanoparticles remained in the site while they were cleared in the healthy tissues (44). MCP-1 magnetic nanoparticles viability assays (0.1, 0.2, and 0.3 mg Fe/mL culture medium) also show that these dextran-IONPs do not affect the viability of monocytes and 3T3 cells (45).

Toxicity and biocompatibility studies of IONPs targeting monocytes-macrophages with other moieties yielded similar results as dextran-IONPs. Cy5.5-OPN-DMSA-IONPs had low cytotoxicity from 5-50 μg/mL on 265.7 macrophages. Additionally, terminal deoxynucleotidyl transferase dUTP nick end labeling (TUNEL) and flow cytometry assays showed that the nanoprobes had insignificant influence on the apoptosis of macrophages (47). CellTiter 96® AQueous one solution cell proliferation assay (MTS) suggested that HA-NWs (0.0625, 0.125, 0.25, 0.5, 1 mg/mL) did not affect viability of vascular endothelial EA.hy926 cells. Furthermore, biocompatibility and histopathological analysis performed post-injection (8 mg Fe/kg) of the nanowires did not show any signs of toxicity on mouse major organs (51).

MTT assays of IONPs targeting VSMCs through Profilin-1 showed no significant effect on VSMCs and macrophage viability after 24h incubation, even at concentrations as high as 0.5 mg/mL (63). Promising results have been obtained from toxicity assays performed with activated platelet targeted IONPs (71,72). *In vivo* toxicity studies of Fe_3O_4-PLGA-cRGD in rats (1 mL, 1mg/mL) obtained no evident effect on blood composition, liver or kidney function post-injection (71). *In vitro* cytotoxicity of EGFP-EGF1-IONPs was determined using CCK-8 assay on U87MG cells and HUVECs. Results suggest that there was no obvious cytotoxicity on both cell types in the studied concentration range (protein or iron 0–50 μg/mL) (80).

In vitro and *in vivo* studies reviewed herein provide evidence that IONPs were well-tolerated by a variety of cell lines and were therefore non-toxic under conditions tested. However, other targeted IONPs should also be investigated to ensure safety and further studies are needed in order to evaluate long-term effects.

5. Conclusions and perspectives

The unique properties of IONPs such as paramagnetism, high surface-to-volume ratio, and biocompatibility has led to extensive research for biomedical applications. This review presented the most recent advances in the molecular imaging of atherosclerosis, thrombosis

and MI using IONPs (Table 1). Overall, IONPs reviewed are non-toxic under conditions tested and have been conjugated with different probes in order to develop single or bimodal contrast agents for molecular imaging. Most of the research on IONPs as contrast agents has been focused on MRI. The relaxivity of IONPs critically depends on size, shape and coating. The IONPs discussed had a size range of 6-404.4 nm and a r_2 and r_1 range of 20.1-489 $mM^{-1}s^{-1}$ and 5.3-44.6 $mM^{-1}s^{-1}$, respectively.

Comparing different IONPs has proved to be challenging in this review as not all studies have provided data on the relaxivity of the nanoparticles. While most studies provided information about the signal change, different measures were used, including post/pre-signal ratio, relative signal intensity change, contrast to noise ratio and signal brightness intensity. Therefore, as more novel IONPs are developed, it is important that researchers provide these data with a qualitative and standardised measurement of signal intensity change.

Most of the IONPs have been designed to target the monocyte-macrophage system, either passively or by targeting macrophages with dextran, D-mannose, PLL, and antibodies. There are concerns of misleading diagnosis in the clinic since macrophages will localize to most inflammatory responses within the body, which could be reduced by the development of IONPs with dual targeting systems to improve the targeting efficacy. Studies reviewed have shown that targeting endothelial cells through E-selectin and VEGFR2, as well as targeting VSMCs via Profilin-1 represent promising strategies for the diagnosis of atherosclerosis. Moreover, activated platelets and fibrin are the most common target markers for thrombosis. Activated platelets have shown to be targeted either through glycoproteins with peptides (RGD) or antibodies (scFv and anti-IgG4), or through other proteins such as P-selectin and Tissue Factor with fucoidan and EGF, respectively. Peptides targeting fibrin include CREKA and FibPeps. Activated platelets and fibrin have demonstrated to not only be promising targets to diagnose thrombosis but also rate the degree and the age of thrombus, making it easier for clinicians to provide the correct treatment for each patient.

Within the clinical landscape of IONPs used for MRI, the only active IONPs currently being used as MRI contrast agent for the cardiovascular system is ferumoxtran-10 (81,82). Ferumoxides and ferucarbotran were designed for MRI of the liver but have also been tested as cardiovascular MRI contrast agents. Ferumoxides caused severe back pain during administration and was discontinued in 2008 (82). Ferucarbotran was discontinued in 2009 because its enhancement was less efficient than Gadolinium-based agents (83). Ferumoxytol is currently used for treatment of anaemia and under ongoing FDA clinical trials for an alternative contrast medium for MRI. Despite the label change and the FDA's boxed warning added to the Feraheme (ferumoxytol) label in March 2015, radiologists have shown increasing interest in using ferumoxytol as a supplement or alternative to gadolinium. Recent clinical trials data suggest ferumoxytol is a safe and promising contrast agent for MRI, especially for imaging the nervous and the cardiovascular system (84). Serious adverse events appear to be rare. With proper precautions, ferumoxytol may be a valuable MR imaging agent.

While some studies have shown their effectiveness as contrast agents in molecular imaging, many of the studies are yet to undertake *in vivo* or *in vitro* testing for biocompatibility. There are potential hazards and complications to address. The potential impact of accumulation of these agents in tissues and their elimination routes have not been studied thoroughly yet. In addition, one of the biggest hurdles for any of these agents is the delivery in enough quantities to enable imaging. Therefore, strategies for overcoming these challenges are required. By understanding these clinically observed limitations, ongoing research and clinical trials are currently being performed to design improved IONPs. As a consequence, limitations are being reduced and clinical acceptance is expected to increase.

Acknowledgement
This work is funded by National Health and Medical Research Council (HTT: APP1037310, APP1182347), Heart Foundation (HTT: 102761), and the University of Queensland (KXVP: Research Training Scholarship).

Disclosure
Nothing to declare.

References

1. WHO. Cardiovascular diseases (CVDs). 2017.
2. Varna M, Juenet M, Bayles R, Mazighi M, Chauvierre C, Letourneur D. Nanomedicine as a strategy to fight thrombotic diseases. Future science OA 2015;1:Fso46.
3. Falk E. Pathogenesis of atherosclerosis. Journal of the American College of Cardiology 2006;47:C7-C12.
4. Mackman N. Triggers, targets and treatments for thrombosis. Nature 2008;451:914-918.
5. Rostam MA, Kamato D, Piva TJ, Zheng W, Little PJ, Osman N. The role of specific Smad linker region phosphorylation in TGF-beta mediated expression of glycosaminoglycan synthesizing enzymes in vascular smooth muscle. Cell Signal 2016;28:956-966.
6. Sato K, Yoshizawa H, Seki T et al. Chemerin-9, a potent agonist of chemerin receptor (ChemR23), prevents atherogenesis. Clin Sci 2019;133:1779-1796.
7. Wang T, Butany J. Pathogenesis of atherosclerosis. Diagn Histopathol 2017;23:473-478.
8. Yusof NNM, McCann A, Little PJ, Ta HT. Non-invasive imaging techniques for the differentiation of acute and chronic thrombosis. Thromb Res 2019;177:161-171.
9. Bentzon FJ, Otsuka FF, Virmani FR, Falk FE. Mechanisms of plaque formation and rupture. Circ Res 2014;114:1852-1866.
10. Nishimoto K, Mimura A, Aoki M, Banura N, Murase K. Application of magnetic particle imaging to pulmonary imaging using nebulized magnetic nanoparticles: Phantom and small animal experiments. Open J Med Imaging 2015;5:49-55.
11. Wadajkar AS, Santimano S, Rahimi M, Yuan B, Banerjee S, Nguyen KT. Deep vein thrombosis: Current status and nanotechnology advances. Biotechnol Adv 2013;31:504-513.
12. Koupenova M, Kehrel BE, Corkrey HA, Freedman JE. Thrombosis and platelets: an update. Eur Heart J 2016;38:785-791.
13. Olaf M, Cooney R. Deep Venous Thrombosis. Emergency medicine clinics of North America 2017;35:743-770.
14. Lu L, Liu M, Sun R, Zheng Y, Zhang P. Myocardial infarction: Symptoms and treatments. Cell Biochem Biophys 2015;72:865-867.
15. Aziz M, Yadav K. Pathogenesis of atherosclerosis. Med Clin Rev 2016;2.
16. Ta HT, Li Z, Hagemeyer CE et al. Molecular imaging of activated platelets via antibody-targeted ultra-small iron oxide nanoparticles displaying unique dual MRI contrast. Biomaterials 2017;134:31-42.
17. Tong S, Hou S, Zheng Z, Zhou J, Bao G. Coating optimization of superparamagnetic iron oxide nanoparticles for high T 2 relaxivity. Nano Letters 2010;10:4607-4613.
18. Siegel-Axel DI, Gawaz M. Platelets and endothelial cells. Semin Thromb Hemost 2007;33:128-135.
19. Arndt N, Tran HD, Zhang R, Xu ZP, Ta HT. Different Approaches to Develop Nanosensors for Diagnosis of Diseases. Advanced Science 2020:2001476.
20. Liu Y, Wu Y, Zhang R et al. Investigating the Use of Layered Double Hydroxide Nanoparticles as Carriers of Metal Oxides for Theranostics of ROS-Related Diseases. ACS Applied Bio Materials 2019;2:5930-5940.
21. Zhang Y, Koradia A, Kamato D, Popat A, Little PJ, Ta HT. Treatment of atherosclerotic plaque: perspectives on theranostics. Journal of Pharmacy and Pharmacology 2019;71:1029-1043.
22. Ta HT, Li Z, Hagemeyer C et al. Novel bionanotechnological solutions based on metal oxide and metal to preserve and assess organs for transplantation. Cryobiology 2018;81:233.
23. Gaston E, Fraser JF, Xu ZP, Ta HT. Nano-and micro-materials in the treatment of internal bleeding and uncontrolled hemorrhage. Nanomedicine: Nanotechnology, Biology and Medicine 2018;14:507-519.
24. Schneider MGM, Lassalle VL. Magnetic iron oxide nanoparticles as novel and efficient tools for atherosclerosis diagnosis. Biomed Pharmacother 2017;93:1098-1115.

25. Ta HT, Li Z, Wu Y et al. Effects of magnetic field strength and particle aggregation on relaxivity of ultra-small dual contrast iron oxide nanoparticles. Materials Research Express 2017;4:116105.
26. Ta H, Li Z, Hagemeyer C et al. Self-confirming molecular imaging of activated platelets via iron oxide nanoparticles displaying unique dual MRI contrast. Atherosclerosis 2017;263:e146.
27. Wu Y, Yang Y, Zhao W et al. Novel iron oxide–cerium oxide core–shell nanoparticles as a potential theranostic material for ROS related inflammatory diseases. Journal of Materials Chemistry B 2018;6:4937-4951.
28. Hagemeyer CE, Alt K, Johnston AP et al. Particle generation, functionalization and sortase A–mediated modification with targeting of single-chain antibodies for diagnostic and therapeutic use. nature protocols 2015;10:90-105.
29. Ta HT, Prabhu ES, Leitner EE et al. Enzymatic Single-Chain Antibody Tagging: A Universal Approach to Targeted Molecular Imaging and Cell Homing in Cardiovascular Disease. Circ Res 2011;109:365-373.
30. Jacques V, Dumas S, Sun W-C, Troughton JS, Greenfield MT, Caravan P. High-relaxivity magnetic resonance imaging contrast agents. Part 2. Optimization of inner- and second-sphere relaxivity. Invest Radiol 2010;45:613-624.
31. Kooi ME, Cappendijk V, Cleutjens K et al. Accumulation of ultrasmall superparamagnetic particles of iron oxide in human atherosclerotic plaques can be detected by in vivo magnetic resonance imaging. Circulation 2003;107:2453-2458.
32. Makowski MR, Varma G, Wiethoff AJ et al. Noninvasive assessment of atherosclerotic plaque progression in ApoE−/− mice using susceptibility gradient mapping. Circ Cardiovasc Imaging 2011;4:295-303.
33. Owens III DE, Peppas NA. Opsonization, biodistribution, and pharmacokinetics of polymeric nanoparticles. Int J Pharm 2006;307:93-102.
34. Suk JS, Xu Q, Kim N, Hanes J, Ensigna LM. PEGylation as a strategy for improving nanoparticle-based drug and gene delivery. Adv Drug Deliv Rev 2016;99:28-51.
35. Ishida T, Kiwada H. Accelerated blood clearance (ABC) phenomenon upon repeated injection of PEGylated liposomes. Int J Pharm 2008;354:56-62.
36. Im HJ, England CG, Feng L et al. Accelerated blood clearance phenomenon reduces the passive targeting of PEGylated nanoparticles in peripheral arterial disease. ACS Appl Mater Interfaces 2016;8:17955-17963.
37. England CG, Im HJ, Feng L et al. Re-assessing the enhanced permeability and retention effect in peripheral arterial disease using radiolabeled long circulating nanoparticles. Biomaterials 2016;100:101-109.
38. Zia A, Wu Y, Nguyen T, Wang X, Peter K, Ta HT. The Choice of Targets and Ligands for Site-Specific Delivery of Nanomedicine to Atherosclerosis. Cardiovasc Res 2020.
39. Tarudji AW, Kievit FM. Active targeting and transport. Nanoparticles for Biomedical Applications: Elsevier, 2020:19-36.
40. Ma L, Liu T-W, Wallig MA et al. Efficient targeting of adipose tissue macrophages in obesity with polysaccharide nanocarriers. ACS nano 2016;10:6952-6962.
41. Yilmaz A, Dengler MA, van der Kuip H et al. Imaging of myocardial infarction using ultrasmall superparamagnetic iron oxide nanoparticles: a human study using a multi-parametric cardiovascular magnetic resonance imaging approach. Eur Heart J 2013;34:462-475.
42. Sosnovik ED, Nahrendorf EM, Deliolanis EN et al. Fluorescence Tomography and Magnetic Resonance Imaging of Myocardial Macrophage Infiltration in Infarcted Myocardium In Vivo. Circulation 2007;115:1384-1391.
43. Stein-Merlob AF, Hara T, McCarthy JR et al. Atheroma susceptible to thrombosis exhibit impaired endothelial permeability in vivo as assessed by nanoparticle-based fluorescence molecular imaging. Circ Cardiovasc Imaging 2017;10:85-92.

44. Barros A, Chacko A-M, Mikitsh J et al. Assessment of global cardiac uptake of radiolabeled iron oxide nanoparticles in apolipoprotein-E-deficient mice: implications for imaging cardiovascular inflammation. Mol Imaging Biol 2014;16:330-339.
45. Kao CW, Wu PT, Liao MY et al. Magnetic nanoparticles conjugated with peptides derived from monocyte chemoattractant protein-1 as a tool for targeting atherosclerosis. Pharmaceutics 2018;10:62-79.
46. Bidder M, Shao J-S, Charlton-Kachigian N, Loewy AP, Semenkovich CF, Towler DA. Osteopontin transcription in aortic vascular smooth muscle cells is controlled by glucose-regulated upstream stimulatory factor and activator protein-1 activities. J Biol Chem 2002;277:44485-44496.
47. Qiao H, Wang Y, Zhang R et al. MRI/optical dual-modality imaging of vulnerable atherosclerotic plaque with an osteopontin-targeted probe based on Fe3O4 nanoparticles. Biomaterials 2017;112:336-345.
48. Liu R, He Y, Li B et al. Tenascin-C produced by oxidized LDL-stimulated macrophages increases foam cell formation through Toll-like receptor-4. Mol Cells 2012;34:35-41.
49. Li Y, Liu J, Huang J-W, Song J-C, Ma Z-L, Shi H-B. In vivo MRI detection of atherosclerosis in ApoE-deficient mice by using tenascin-C-targeted USPIO. Acta Radiol 2018;59:1431-1437.
50. Vendrov AE, Madamanchi NR, Niu X-L et al. NADPH oxidases regulate CD44 and hyaluronic acid expression in thrombin-treated vascular smooth muscle cells and in atherosclerosis. J Biol Chem 2010;285:26545-26557.
51. Hossaini Nasr S, Tonson A, El-Dakdouki MH et al. Effects of nanoprobe morphology on cellular binding and inflammatory responses: hyaluronan-conjugated magnetic nanoworms for magnetic resonance imaging of atherosclerotic plaques. ACS Appl Mater Interfaces 2018;10:11495-11507.
52. Ta HT, Truong NP, Whittaker AK, Davis TP, Peter K. The effects of particle size, shape, density and flow characteristics on particle margination to vascular walls in cardiovascular diseases. Expert Opin Drug Deliv 2018;15:33-45.
53. Tarin C, Carril M, Martin-Ventura JL et al. Targeted gold-coated iron oxide nanoparticles for CD163 detection in atherosclerosis by MRI. Sci Rep 2015;5:1-9.
54. Kolodgie FD, Petrov A, Virmani R et al. Targeting of apoptotic macrophages and experimental atheroma with radiolabeled annexin V: a technique with potential for noninvasive imaging of vulnerable plaque. Circulation 2003;108:3134-3139.
55. Cheng D, Li X, Zhang C et al. Detection of vulnerable atherosclerosis plaques with a dual-modal single-photon-emission computed tomography/magnetic resonance imaging probe targeting apoptotic macrophages. ACS Appl Mater Interfaces 2015;7:2847-2855.
56. Varasteh Z, Mohanta S, Li Y et al. Targeting mannose receptor expression on macrophages in atherosclerotic plaques of apolipoprotein E-knockout mice using 68 Ga-NOTA-anti-MMR nanobody: non-invasive imaging of atherosclerotic plaques. EJNMMI research 2019;9:40-45.
57. Babič M, Schmiedtová M, Poledne R, Herynek V, Horák D. In vivo monitoring of rat macrophages labeled with poly(l‐lysine)‐iron oxide nanoparticles. J Biomed Mater Res B 2015;103:1141-1148.
58. Kang HW, Josephson L, Petrovsky A, Weissleder R, Bogdanov A. Magnetic resonance imaging of inducible E-selectin expression in human endothelial cell culture. Bioconjugate Chem 2002;13:122-127.
59. Kang HW, Torres D, Wald L, Weissleder R, Bogdanov Jr AA. Targeted imaging of human endothelial-specific marker in a model of adoptive cell transfer. Lab Invest 2006;86:599-609.
60. Camaré C, Pucelle M, Nègre-Salvayre A, Salvayre R. Angiogenesis in the atherosclerotic plaque. Redox Biol 2017;12:18-34.
61. Chen H, Chen L, Liang R, Wei J. Ultrasound and magnetic resonance molecular imaging of atherosclerotic neovasculature with perfluorocarbon magnetic nanocapsules targeted

against vascular endothelial growth factor receptor 2 in rats. Mol Med Rep 2017;16:5986-5996.
62. Peterson SM, Turner JE, Harrington A et al. Notch2 and Proteomic Signatures in Mouse Neointimal Lesion Formation. Arterioscl Thromb Vas 2018;38:1576-1593.
63. Wang Y, Cao F. In vivo MR and fluorescence dual-modality imaging of atherosclerosis characteristics in mice using profilin-1 targeted magnetic nanoparticles. Journal of the American College of Cardiology 2016;68:272-286.
64. Ta HT, Prabhu S, Leitner EE et al. Targeted molecular imaging and cell homing in cardiovascular disease via antibody-sortagging. Atherosclerosis 2015;241:e26.
65. Ta HT, Peter K, Hagemeyer CE. Enzymatic antibody tagging: toward a universal biocompatible targeting tool. Trends Cardiovasc Med 2012;22:105-11.
66. Ta HT, Prabhu S, Leitner E et al. Antibody-sortagging: a universal approach towards targeted molecular imaging and cell homing in cardiovascular disease. Circ Res 2010;107:e37-e38.
67. Jacobin-Valat M-J, Laroche-Traineau J, Larivière M et al. Nanoparticles functionalised with an anti-platelet human antibody for in vivo detection of atherosclerotic plaque by magnetic resonance imaging. Nanomedicine 2015;11:927-937.
68. Bachelet L, Bertholon I, Lavigne D et al. Affinity of low molecular weight fucoidan for P-selectin triggers its binding to activated human platelets. Biochimica et biophysica acta 2009;1790:141-146.
69. Suzuki M, Bachelet-Violette L, Rouzet F et al. Ultrasmall superparamagnetic iron oxide nanoparticles coated with fucoidan for molecular MRI of intraluminal thrombus. Nanomedicine 2015;10:73-87.
70. Smith LL, Cheung H-K, Ling LE et al. Osteopontin N-terminal domain contains a cryptic adhesive sequence recognized by α9β1 integrin. J Biol Chem 1996;271:28485-28491.
71. Liu J, Xu J, Zhou J, Zhang Y, Guo D, Wang Z. Fe3O4-based PLGA nanoparticles as MR contrast agents for the detection of thrombosis. Int J Biomed 2017;12:1113-1126.
72. Hu Y, Li Z, Shi W et al. Early diagnosis of cerebral thrombosis by EGFP–EGF1 protein conjugated ferroferric oxide magnetic nanoparticles. J Biomater Appl 2019:1195-1201.
73. Mori H, Kolodgie FD, Finn AV, Virmani R. Pathology and Pathophysiology of Coronary Atherosclerotic Plaques. CT of the Heart: Springer, 2019:211-226.
74. Starmans LW, Moonen RP, Aussems-Custers E et al. Evaluation of iron oxide nanoparticle micelles for magnetic particle imaging (MPI) of thrombosis. PLoS one 2015;10:e0119257.
75. Stefanelli VL, Barker TH. The evolution of fibrin-specific targeting strategies. J Mater Chem B 2015;3:1177-1186.
76. Poon C, Gallo J, Joo J, Chang T, Bañobre-López M, Chung EJ. Hybrid, metal oxide-peptide amphiphile micelles for molecular magnetic resonance imaging of atherosclerosis. J Nanotechnol 2018;16:92-103.
77. Ta H, Arndt N, Wu Y et al. Activatable magnetic resonance nanosensor as a potential imaging agent for detecting and discriminating thrombosis. Nanoscale 2018:15103-15115.
78. Ta HT. Activatable Magnetic Resonance Nanosensor as a Potential Imaging Agent for Detecting and Discriminating Thrombosis. Atherosclerosis 2019;32:159.
79. Yang K, Hu L, Ma X et al. Multimodal Imaging Guided Photothermal Therapy using Functionalized Graphene Nanosheets Anchored with Magnetic Nanoparticles. J Adv Mater 2012;24:1868-1872.
80. Liu H, Chen X, Xue W et al. Recombinant epidermal growth factor-like domain-1 from coagulation factor VII functionalized iron oxide nanoparticles for targeted glioma magnetic resonance imaging. Int J Nanomedicine 2016;11:5099.
81. Anselmo AC, Mitragotri S. Nanoparticles in the clinic. Bioengineering & Transla Med 2016;1:10-29.
82. Anselmo AC, Mitragotri S. Nanoparticles in the clinic: An update. Bioeng Transl Med 2019;4:e10143.

83. Wang Y-XJ. Current status of superparamagnetic iron oxide contrast agents for liver magnetic resonance imaging. World J Gastroenterol 2015;21:13400-13402.
84. Toth GB, Varallyay CG, Horvath A et al. Current and potential imaging applications of ferumoxytol for magnetic resonance imaging. Kidney Int 2017;92:47-66.

Highlights

- Current imaging methods to detect CVDs such as atherosclerotic plaques and thrombosis are mostly invasive.
- Molecular imaging techniques have been developed as a non-invasive approach to image CVDs due to its high spatial resolution and safety.
- A number of studies have shown the effectiveness of iron oxide as single- or multi-modality contrast agents in molecular imaging of atherosclerosis, thrombosis and myocardial infarction.
- Targeting biomarkers on endothelial cells and vascular smooth muscle cells represents a promising strategy for the diagnosis of atherosclerosis while targeting activated platelets and fibrin is promising for thrombosis imaging.
- Many of the studies are yet to undertake comprehensive testing of biocompatibility. There are still potential hazards to address and complications to diagnosis, therefore strategies for overcoming these challenges are required.

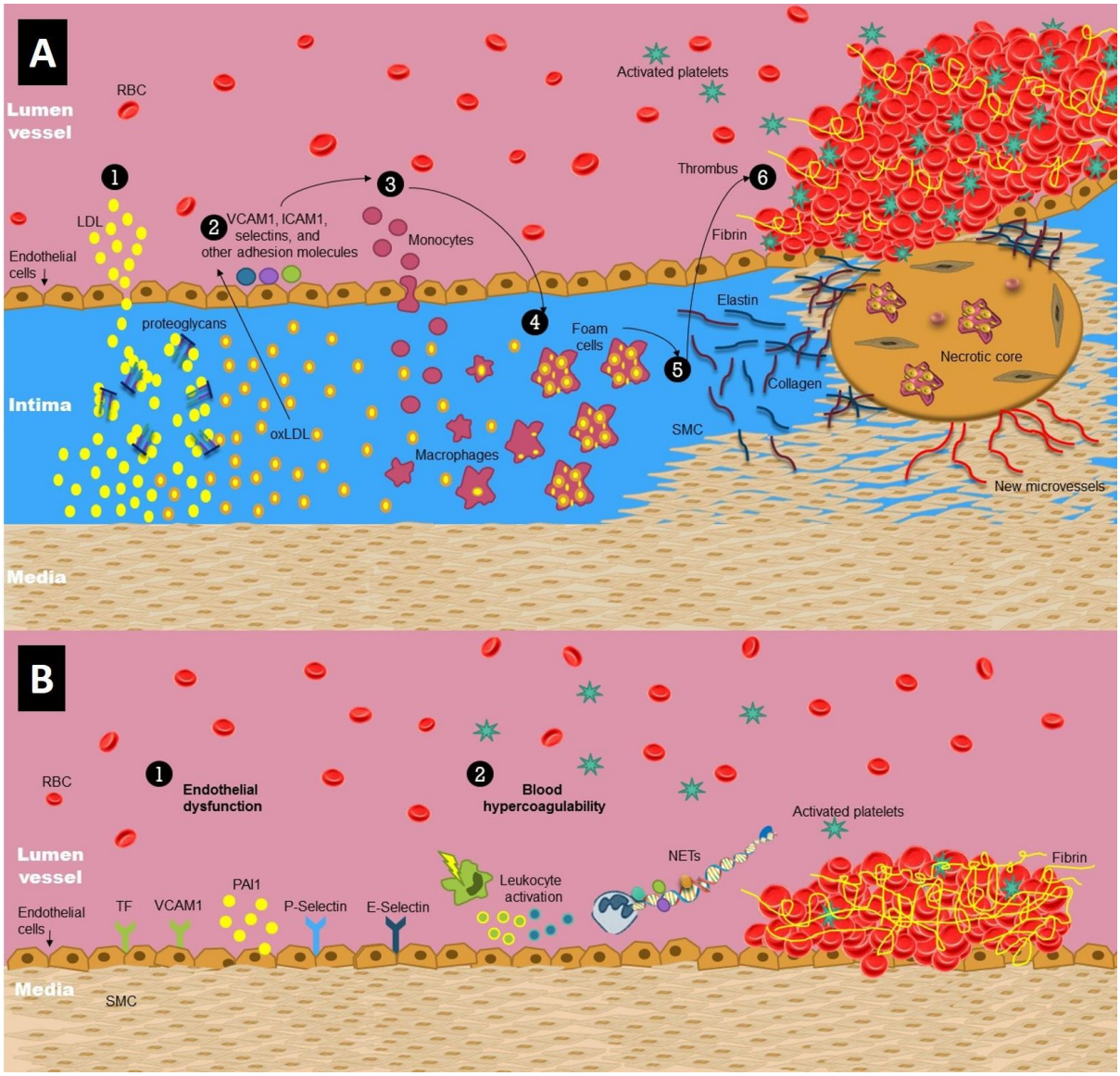

Figure 1 A) Development of atherothrombosis. LDL-cholesterol damages the endothelium and extravasates to the intima, accumulate in proteoglycans, and become oxidized (1). Oxidation stimulates the ECs to produce adhesion molecules (2) that recruit monocytes (3). M-CSF stimulates the differentiation of monocytes into macrophages that ex press SR-A and CD36. Macrophages recognize ox-LDLs and phagocytize them, generating foam cells (4)**.** Smooth muscle cells may migrate to the intima and contribute to foam cells' formation (5). The death of foam cells forms a mass of extracellular lipids, and a fibrous cap of SMC, collagen and elastin. These lead to a necrotic and apoptotic core. If the plaque ruptures, the thrombogenic material is exposed to the lumen, platelets will activate and adhere to the endothelium, forming a thrombus (6) (2,3,7,8). **B) Development of Venous thrombosis.** Slow blood flow in the veins might lead to endothelial dysfunction and therefore, expression of cell adhesion molecules such as vascular cell adhesion protein 1 (VCAM1), P-selectin and E-selectin. This might lead to recruitment and activation of leukocytes to the vessel wall, downregulating antithrombotic factors, releasing neutrophil extracellular traps (NETs) upregulating inhibitor 1 (PAI1) and tissue factor (TF). These events trigger the coagulation cascade and accumulation of red blood cells and fibrin, blocking the vessel and causing venous thrombosis (13).

Table 1. IONPs developed for molecular imaging of atherosclerosis, thrombosis and myocardial infarction						
Target	**Size (nm)**	**Relaxivity**	**Binding ligand**	**Target marker**	**Imaging modality**	**Ref.**
Passive targeting	7	r_1=20.1 $mM^{-1}s^{-1}$ r_2=37.1 $mM^{-1}s^{-1}$	citrate	Macrophage-monocyte system	SGM-MRI	(32)
	93	-	PEG	Macrophage-monocyte system	PET NIRF	(36)
Macrophages and monocytes with dextran	30	r_1=15 $mM^{-1}s^{-1}$ r_2=89 $mM^{-1}s^{-1}$	dextran	dextran-binding C-type lectins	MRI cine-CMR	(41)
	-	-	dextran	dextran-binding C-type lectins	Fluorescence tomography MRI	(42)
	30	-	dextran	dextran-binding C-type lectins	Digital autoradiography MRI	(44)
	20-30	-	dextran	dextran-binding C-type lectins	NIRF MRI	(43)
	20-150	-	Dextran and MCP-1	dextran-binding C-type lectins and CCR2	MRI	(45)
Macrophages and monocytes with other moieties	7.3	r_2= 135.2 $mM^{-1}s^{-1}$	OPN antibody	Osteopontin	Fluorescence imaging MRI	(47)
	47	r_2= 168.24 $mM^{-1}s^{-1}$	Tenascin-C antibody	Tenascin-C	MRI	(49)
	HA-SPION 20 HA-NW 65	-	Hyaluronan	CD44	MRI	(51)
	6	-	CD163 antibody	CD163	MRI	(53)
	20	r_1= 8.2 $mM^{-1}s^{-1}$ r_2= 20.1 $mM^{-1}s^{-1}$	Annexin V	Phosphatidyl-serine	SPECT MRI	(55)
	180	-	D-mannose PLL	Mannose receptors	MRI	(57)
Endothelial cells	40.6	-	E-selectin antibody	E-selectin	MRI	(58,59)
	404.4	-	VEGFR2 antibody	VEGFR2	Ultrasound MRI	(61)
Vascular Smooth Muscle cells	30.2	r_2= 134.5 $mM^{-1}s^{-1}$	Profilin-1 antibody	Profilin-1	NIRF MRI	(63)
Activated platelets	-	-	scFv	LIBS epitopes on glycoprotein IIb/IIIa	MRI	(29)

	7.7	r_1= 5.3 $mM^{-1}s^{-1}$ r_2= 73.4 $mM^{-1}s^{-1}$	scFv	LIBS epitopes on glycoprotein IIb/IIIa	MRI	(16)
	7.5	r_2= 273 $mM^{-1}s^{-1}$	rIgG4 TEG4 antibody	glycoproteins αIIB and β3	MRI	(67)
	33.8	r_1= 37.5 $mM^{-1}s^{-1}$ r_2= 137 $mM^{-1}s^{-1}$	Fucoidan	P-selectin	MRI	(69)
	368	-	cRGD	glycoprotein IIb/IIIa	MRI	(71)
Tissue factor	100	-	EGFP-EGF1	Tissue factor	MSFI MRI	(72)
Fibrin	40	r_1= 5.6 $mM^{-1}s^{-1}$ r_2= 207 $mM^{-1}s^{-1}$	FibPep (cyclic RWQPCPAE SWT-Cha-CWDP)	Fibrin	MRI	(74)
	20-30	r_2= 457 $mM^{-1}s^{-1}$	CREKA	Fibrin	MRI	(76)
	160	r_1= 44.6 $mM^{-1}s^{-1}$ r_2= 489 $mM^{-1}s^{-1}$	FibPep (GPRPPGGS[Lys(TMR)]GC)	Fibrin	MRI	(77)